

# “Comets” orbiting a black hole

R. Maiolino<sup>1</sup>, G. Risaliti<sup>2,3</sup>, M. Salvati<sup>2</sup>, P. Pietrini<sup>4</sup>, G. Torricelli-Ciamponi<sup>2</sup>, M. Elvis<sup>3</sup>, G. Fabbiano<sup>3</sup>, V. Braito<sup>5,6</sup>, and J. Reeves<sup>7</sup>

<sup>1</sup> INAF-Osservatorio Astronomico di Roma, via di Frascati 33, 00040 Monte Porzio Catone, Italy

<sup>2</sup> Osservatorio Astrofisico di Arcetri, Largo E. Fermi 5, 50125 Firenze, Italy

<sup>3</sup> Harvard-Smithsonian Center for Astrophysics, 60 Garden St. Cambridge, MA 02138 USA

<sup>4</sup> Dipartimento di Astronomia, Università di Firenze, largo E. Fermi 2, 50125 Firenze, Italy

<sup>5</sup> Department of Physics and Astronomy, University of Leicester, University Road, Leicester, LE1 7RH, UK

<sup>6</sup> Department of Physics and Astronomy, Johns Hopkins University, Baltimore, MD 21218

<sup>7</sup> Astrophysics Group, School of Physical and Geographical Science, Keele University, Keele, Staffordshire ST5 5BG, UK

Received ; accepted

## ABSTRACT

We use a long (300 ksec), continuous *Suzaku* X-ray observation of the active nucleus in NGC 1365 to investigate the structure of the circumnuclear BLR clouds through their occultation of the X-ray source. The variations of the absorbing column density and of the covering factor indicate that the clouds surrounding the black hole are far from having a spherical geometry (as sometimes assumed), instead they have a strongly elongated and cometary shape, with a dense head ( $n \sim 10^{11} \text{ cm}^{-3}$ ) and an expanding, dissolving tail. We infer that the cometary tails must be longer than a few times  $10^{15} \text{ cm}$  and their opening angle must be smaller than a few degrees. We suggest that the cometary shape may be a common feature of BLR clouds in general, but which has been difficult to recognize observationally so far. The cometary shape may originate from shocks and hydrodynamical instabilities generated by the supersonic motion of the BLR clouds into the intracloud medium. As a consequence of the mass loss into their tail, we infer that the BLR clouds probably have a lifetime of only a few months, implying that they must be continuously replenished. We also find a large, puzzling discrepancy (two orders of magnitude) between the mass of the BLR inferred from the properties of the absorbing clouds and the mass of the BLR inferred from photoionization models; we discuss the possible solutions to this discrepancy.

**Key words.** Galaxies: Individual: NGC 1365 – Galaxies: Seyfert — Galaxies: nuclei; X-rays: galaxies

## 1. Introduction

The variability of the absorbing gaseous column density  $N_{\text{H}}$  observed in the X-ray spectra of Active Galactic Nuclei have revealed that a significant fraction of the absorbing medium must be clumpy (Risaliti et al., 2002). Moreover,  $N_{\text{H}}$  variations on time scales as short as a few days or hours have shown that a significant fraction of such absorbing clouds must be located very close to the nuclear X-ray source (Elvis et al., 2004; Risaliti et al., 2005a; Puccetti et al., 2007) and, more specifically, within the Broad Line Region (BLR).

The nucleus of the galaxy NGC 1365 is amongst the sources that were investigated more thoroughly in this respect, thanks to its brightness and probably also to a fortunate (intermediate) inclination of the absorbing medium relative to our line of sight. This is a nearby ( $z=0.0055$ ) type 1.8 Seyfert galaxy that was observed several times in the X-rays, and displayed strong column density variations on time scales as short as a few days (e.g. Risaliti et al., 2005a, 2007). Most of the observations had probed absorption variations of this source in discrete, non-contiguous time intervals. More recently, (nearly) continuous XMM observations of NGC 1365 were presented in Risaliti et al. (2009a) and in Risaliti et al. (2009b). In particular, the latter observation allowed the continuous monitoring of an absorption event lasting about 40 ksec, which was modelled with a cloud partially eclipsing the X-ray source. More specifically, the spectral variations were modelled by assuming a constant column density of the absorber ( $N_{\text{H}} \sim 3.5 \cdot 10^{23} \text{ cm}^{-2}$ ) and a variable covering factor. The inferred density, velocity and distance from the black

hole of the variable absorber is strikingly similar to those of the BLR clouds. The complex spectrum always requires a foreground non-variable (or very slowly variable) absorber ( $N_{\text{H}} \sim$  a few times  $10^{22} \text{ cm}^{-2}$ ), totally covering the source, possibly associated with gas at larger distances from the nucleus (possibly in the host galaxy).

NGC 1365 has also been observed with *Suzaku* (Mitsuda et al., 2007) with a continuous observation lasting more than 300 ksec. The integrated spectrum was already presented in Risaliti et al. (2009c), mostly focusing on the high energy part obtained with the Hard X-ray Detector (HXD), and revealing an unusually strong excess of emission at  $E > 10 \text{ keV}$ . Such excess is ascribed to X-ray radiation piercing a partial, Compton thick ( $N_{\text{H}} \sim 4 \times 10^{24} \text{ cm}^{-2}$ ) absorber. The high energy excess appears stable over long time scales (Risaliti et al., 2000, 2009c). The emerging scenario is that three distinct absorbers are present: (1) a distant absorber with  $N_{\text{H}} < 10^{23} \text{ cm}^{-2}$ , probably associated with gas in the host galaxy; (2) an absorber made of broad line region (BLR) clouds with  $N_{\text{H}} \sim 10^{23-24} \text{ cm}^{-2}$  rapidly orbiting around the black hole; (3) an absorber with  $N_{\text{H}} \sim 4 \times 10^{24} \text{ cm}^{-2}$  partially covering the source, consisting either of the outer region of a warped accretion disk, or of a large number of small ( $< 10^{12} \text{ cm}$ ) and dense ( $n > 10^{12} \text{ cm}^{-3}$ ) clouds located in the vicinity of the accretion disk.

In this paper we focus on the absorption variations in the spectral range 2-10 keV, ascribed to BLR clouds passing along the line of sight, through a detailed temporal analysis of the spectra provided by the *Suzaku* low energy (XIS) data of NGC 1365.

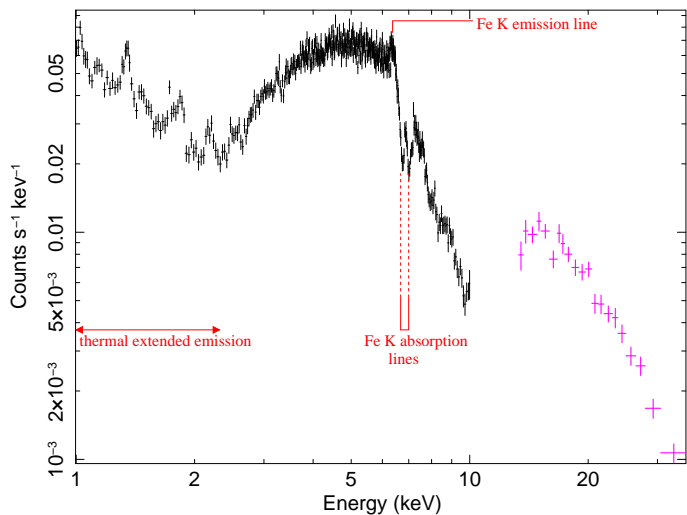


**Fig. 1.** Merged XIS0 and XIS3 spectra (1–10 keV) and HXD spectrum (15–60 keV) of NGC 1365, integrated over the whole duration of the observation. No spectral fit is shown since, as discussed in the text, the absorption components are highly variable, hence a fit (with constant components) to the total, time-averaged spectrum is meaningless.

We identify two eclipsing events that we can model in detail in terms of variations of both covering factor and column density. The time variations of these quantities are highly asymmetric and strongly suggest that the absorbing clouds have a cometary shape, i.e. a well defined head and a more diffuse elongated, conical, tail.

## 2. Observations and data reduction

The observations and the basic data reduction were already reported in Risaliti et al. (2009c). In this section we only briefly summarize the observations and data reduction of the X-ray Imaging Spectrometer (XIS Koyama et al., 2007) data.

The observations were performed on 2007 January 21–25, for an elapsed time of about 320 ksec and a net exposure of 160 ksec. The spectra and calibrations were obtained following the standard procedure described in the *Suzaku* reduction guide. The XIS spectra and light curves were extracted in a region with a radius of 2.9 arcmin (i.e. matching the optimized aperture for the arf matrix) around the nucleus of NGC 1365. The background was extracted in a region far from the source, with the same radius adopted for the source extraction. The calibration files were produced by using the FTOOLS 6.6 package. The reduction of the Hard X-ray Detection (HXD) data, only marginally used in this paper, is discussed in Risaliti et al. (2009c).

## 3. Temporal and spectral analysis

In this paper the spectra from the three CCDs (XIS0, XIS1 and XIS3) are always treated separately, especially in the statistical analysis. However, for sake of clarity, some of the figures will show the merged spectra or light curves, for illustrative purposes only.

In the 0.5–10 keV range during the whole observation the three XIS collected a total of about  $2 \cdot 10^5$  photons. Fig. 1 shows the XIS0 and XIS3 merged spectrum integrated over the whole observation along with the HXD spectrum. No spectral fit is

shown for the total, time-averaged spectrum, since the strong spectral variability (especially of the absorption components) over the entire observation, as discussed in the following, makes any fit with constant components of the integrated spectrum meaningless (as also discussed in Risaliti et al., 2009b).

Fig. 2a shows the combined light curve in the 2–5 keV band rebinned to 2.880 ksec (about half of the *Suzaku* orbital period). The light curve shows strong variations even on short timescales of a few ksec, including two sharp drops (marked A and B in Fig. 2) that are strongly reminiscent of the eclipse events seen in Chandra and XMM. The egress from these “eclipses” is less clear cut however, suggesting more complex structure in the absorber.

To investigate the nature of these variations we have extracted the X-ray spectra in 12 time intervals, selected either to match the main variations of the light curve or by simply dividing long time intervals into equally spaced sub-intervals. Within each time interval the light curve generally shows additional structures, but we decided not to further split the time intervals for the extraction of the spectra, since the resulting poorer statistics would make the errors on the fitting parameters too large, or would introduce strong degeneracy between some of them. On average, each time interval contains about  $1.5 \cdot 10^4$  photons (e.g. Fig. 3).

The resulting 36 spectra (for each time interval there are 3 spectra, XIS0, XIS1 and XIS3) are simultaneously fitted with a model consisting of multiple components, quite similar to previous modelling of the same source (Risaliti et al., 2009b; Guainazzi et al., 2009), with most components and parameters held constant for all time intervals (and hence constrained by the full statistics of  $2 \cdot 10^5$  photons) and a few parameters left free to vary for the different time intervals. In the following we summarize the various models components.

1. *Soft thermal components.* As reviewed and discussed in Guainazzi et al. (2009) the soft part of the spectrum (0.5–2 keV) is ascribed to a complex combination of hot plasmas present in the circumnuclear star forming regions (Wang et al., 2009) and in the Narrow Line Region cones, as well as the contribution from point sources (X-ray binaries and Ultra Luminous X-ray sources, Soria et al., 2009). Following the detailed analysis in Guainazzi et al. (2009) we fit the soft spectrum with three components: two absorbed thermal plasmas (“mekal” in XSpec) and a black-body. The resulting best fit parameters are generally in agreement with those obtained by Guainazzi et al. (2009) (see below), keeping in mind that the aperture adopted here is different, hence we do not expect an exact match. However, the details of these soft components are unimportant within the context of this paper, since they are constant in time and do not affect the variability observed in the 2–10 keV spectral region.
2. *Powerlaw and two cold absorbers.* The bulk of the 2–10 keV emission is due to a primary powerlaw component, ascribed to the corona surrounding the black hole accretion disk, with a double absorber: one absorber ( $N_{H,1}$ ) totally covering the X-ray source, which we shall ascribe to a foreground medium far from the X-ray source, and a second absorber ( $N_{H,2}$ ) partially covering the source, which, following Risaliti et al. (2009b), we shall ascribe to clouds transiting close to the X-ray source (probably BLR clouds). By using wider time intervals ( $\sim 50$  ksec) we found that the spectral index does not change within the errors (as also found by Risaliti et al., 2009b). Therefore, we assumed that the spectral index is the same for all 12 time intervals. The powerlaw

normalization is left free to vary among the time intervals. The first, total, absorber is kept constant for all time intervals. The absorber with partial covering is left free to vary both in terms of column density ( $N_{\text{H},2}$ ) and in terms of covering factor (CF).

3. *Narrow FeK line.* A narrow (unresolved) iron FeK $\alpha$  line at  $\sim 6.4$  keV is clearly detected. In larger temporal bins the flux of this line is not observed to vary. As discussed by various previous works the narrow FeK line is probably produced by circumnuclear dense clouds (most likely Broad Line Clouds and circumnuclear absorbing medium in general). The parameters of this line are therefore kept constant and fitted simultaneously for all time intervals.
4. *Broad FeK line.* As discussed in Risaliti et al. (2009b) the spectrum of NGC 1365 (when not in a Compton thick state) also requires a broad, relativistic iron FeK $\alpha$  line. The parameters of the iron line (fitted with the “laor” function within Xspec) are kept constant for all time intervals, except for its normalization that is required to be proportional to the primary powerlaw in each time interval (i.e. constant equivalent width). The physical justification of this assumption is that, according to standard models, the relativistically broadened iron line comes from a very small region, of the order of a few Schwarzschild radii, ( $M_{\text{BH}} \sim 2 \cdot 10^6 M_{\odot}$ , hence  $R_{\text{S}} \sim 6 \cdot 10^{11}$  cm, Risaliti et al., 2009b) and therefore it should respond to the continuum variations on timescales much shorter ( $\sim 100$  sec) than the size of our time intervals. However, in a few representative intervals we have tried to leave the normalization of the broad line free, and the fitting results do not change significantly, the main effect being mostly that the confidence intervals increase by about 20–30%.
5. *FeXXV and FeXXVI absorption lines.* As first discovered by Risaliti et al. (2005b) the spectrum of NGC 1365 is characterized by a set of four absorption lines at  $\sim 7$  keV due to Fe XXV and Fe XXVI, both K $\alpha$  and K $\beta$ . These lines are also clearly detected in our *Suzaku* spectrum (Fig. 1). As in Risaliti et al. (2005b), the depth of each absorption line is left free to vary independently in each time interval, but the four lines are required to have the same velocity shift within each interval. We note that given the high ionization state of this absorber, its only spectral components that we expect to be important are just the Fe absorption lines, i.e. there is no significant continuum photoelectric absorption associated with this absorber.
6. *Reflection components.* As in Risaliti et al. (2009b) the fit also includes a set of three (constant in time) continuum reflection components: i) a power law with the same spectral index as the primary continuum, which accounts for the free electron scattering by an ionized reflecting medium on large scale (e.g. hot gas in the Narrow Line Region), hence this component is assumed constant over the whole observation; ii) a cold reflection (modelled with “pexrav” in Xspec), associated with the same medium responsible for the FeK $\alpha$  narrow line emission, likely the circumnuclear dense clouds, hence it is assumed to be constant, as in the case of the narrow FeK; iii) an inner ionized absorber (modelled with “pexriv” in Xspec and subject to the same absorption as the primary power law component) to account for warm reflection due to ionized gas close to the X-ray source, possibly the accretion disk itself; this third component is assumed, as for the broad FeK line, to respond to the continuum variations on timescales much shorter than our time intervals, hence its normalization is assumed to scale proportionally to the

primary powerlaw continuum within each time interval. We will see that the reflection components i) and iii) contribute very little to the global fit. Finally, we note that component iii) may be relativistically blurred, however given its small contribution to the spectrum such “blurring” cannot be constrained and it does not affect the total fit.

7. *Compton thick absorbed powerlaw.* As mentioned in sect. 1, the *Suzaku* spectrum at  $E > 15$ keV (HXD) shows an excess of emission with respect to the extrapolation of the above components Risaliti et al. (2009c). This excess is best interpreted by assuming that the intrinsic X-ray emission is actually stronger than observed in the 2–10 keV spectrum, but partially absorbed by gas very close to the X-ray source that we fit with  $N_{\text{H},3} = 3.7_{-1.0}^{+1.4} 10^{24}$  cm $^{-2}$ . The inferred covering factor strongly depends on the geometry of the Compton thick medium, as discussed in Risaliti et al. (2009c). Compton thick partial covering has also been observed in other sources (Turner et al., 2009). This inner, very thick, partial absorber is either associated with gas in a warped accretion disk or a population of small and dense clouds surrounding the accretion disk. The very high-energy excess is found to be stable over long time scales (years), hence in our analysis of the *Suzaku* data this component was assumed constant for all time intervals. We note that this additional component at high energies does not affect the fitting of  $N_{\text{H},2}$  and CF.

The global, simultaneous fit gives a reduced  $\chi^2_{\nu}=1.055$ . Overall there are 25 free parameters common to all time intervals that, therefore, are constrained by the full  $2 \cdot 10^5$  photon statistics. Each time interval has its own set of 8 free parameters, three for the continuum ( $N_{\text{H},2}$ , CF and powerlaw normalization) and five for the absorption Fe lines (velocity and individual depth).

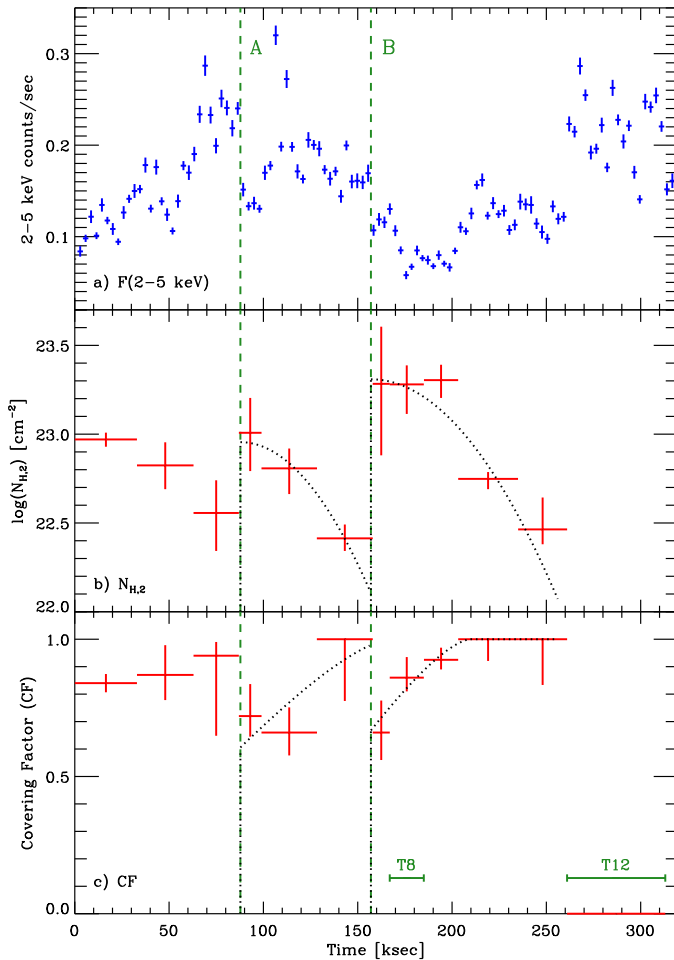
Fig. 3 shows the spectra and the resulting fit in two representative time intervals (T8 and T12, as marked in Fig. 2), clearly displaying a strong variation of absorption between the two time intervals.

In the following we will mostly focus on the variations of the column density  $N_{\text{H},2}$  and of the Covering Factor (CF) of the partial absorber, whose resulting best-fit values in the various time intervals are shown in Fig. 2b and c.

One possible concern is whether these two quantities are degenerate, given the reduced statistics available in each time interval. We found this not to be the case in any of the time intervals (except for the last interval, which does not require a second absorber). As an example, Fig. 4 shows the confidence levels in the  $N_{\text{H},2}$  versus CF plane, for the time interval T8: although there is some correlation between the two parameters around the best solution, the 90% confidence contour provides good constraints on both quantities. We emphasize that this is the first time that a temporally resolved X-ray spectral analysis is able to break the degeneracy between the evolution of the column density ( $N_{\text{H}}$ ) and the covering factor (CF) of the X-ray absorber in an AGN.

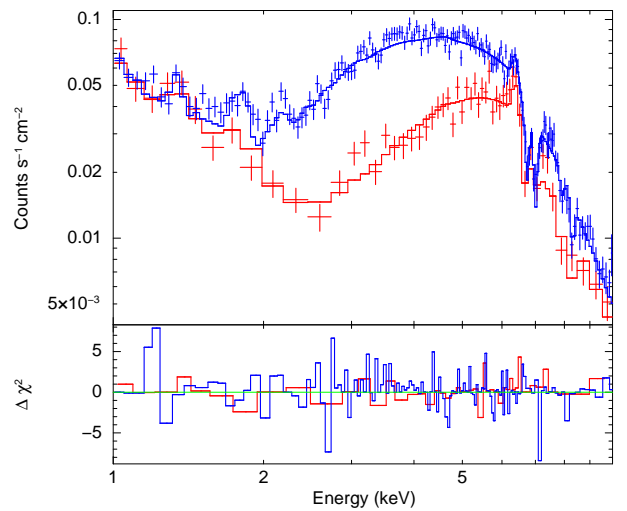
In the rest of this section we report the fitting results for the other parameters, which, although important for the global fit, are less relevant for the topic of this paper.

Table 1 lists the best fitting values for the main parameters in common to all time intervals. The first part reports the soft (not variable) thermal components. The second part reports the powerlaw slope and the reflection components. Note that the continuum slope  $\Gamma$  obtained here is different than obtained by Risaliti et al. (2009c) on the same set of data, i.e.  $\Gamma = 2.34_{-0.02}^{+0.03}$ . There are two clear  $\chi^2$  minima for this parameter, but the detailed analysis in sub-intervals performed here (hence account-



**Fig. 2.** a) Photon count rate in the soft band 2-5 keV as a function of time (in time intervals 2.88 ksec). The vertical, green dashed lines indicate the beginning of the two main eclipses produced by two clouds passing in front of the X-ray source. The vertical errorbars indicate the  $1\sigma$  fluctuations within each bin. b) Column density ( $N_{H,2}$ ) of the variable absorber in the 12 time intervals, resulting from their simultaneous spectral fit. Errorbars on  $N_{H,2}$  are at the 90% confidence. The black dotted lines indicate a quadratic fit to  $N_{H,2}$  in the eclipses “A” and “B”. c) Covering factor (CF) of the variable absorber. Errorbars on CF are at the 90% confidence. The dotted lines show the variation of covering factor expected from the cometary model shown in Fig. 8 and discussed in the text. The segments labelled with T8 and T12 show the extraction time intervals of the spectra shown in Fig. 3.

ing for the spectral variability) shows that the  $\chi^2$  minimum with  $\Gamma = 1.81$  fits the data with much higher significance ( $\chi^2_{\nu} = 1.05$ , versus  $\chi^2_{\nu} = 1.08$ , with about a thousand d.o.f). The reflection factor  $R$  of the reflection components is given relative to the 2–10 powerlaw continuum observed in the last time interval, T12 (Fig. 2). The real value of the reflection factor should be given relative to the intrinsic powerlaw component, i.e. the continuum observed at  $E > 20$  keV corrected for the Compton thick partial covering  $N_{H,3}$ , which is much higher than the component observed in the 2–10 keV range and which gives values of  $R$  that are much lower. However, applying the correction to the continuum transmitted at high energies is very uncertain, since it depends strongly on the geometry of the Compton thick absorbing medium, as discussed in detail in Risaliti et al. (2009c).



**Fig. 3.** Merged XIS0 and XIS3 spectra of NGC 1365 and resulting fitting model in two representative time intervals, T8 (between 167 ksec and 185 ksec, red) and T12 (between 261 ksec and 313 ksec, blue), as indicated in Fig. 2. Although, for the sake of clarity, we plot the combined XIS0 and XIS3 spectra in both figures, in the fitting analysis we used all individual XIS spectra (XIS0, XIS1 and XIS3), kept separate.

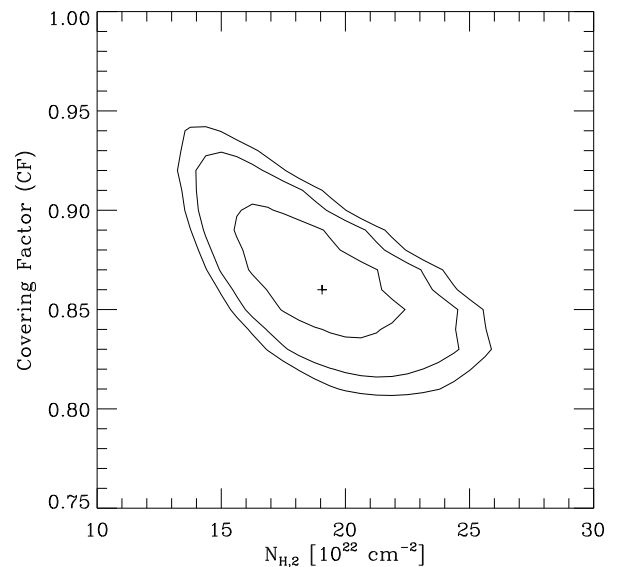


**Fig. 4.** 68%, 90% and 95% confidence levels in the  $N_{H,2}$  versus Covering Factor diagram, for the time interval T8 (Fig. 2). The cross marks the best fit parameters.

The third part of Table 1 reports the constant absorption components. For what concerns the Compton thick absorbing medium,  $N_{H,3}$  only accounts for the photoelectric absorption, which is enough for our purposes, since we are not interested in the high-energy component. The full treatment including the Compton scattering is given in Risaliti et al. (2009c).

The fourth part of Table 1 provides the parameters of the emission lines. The equivalent widths are given relative to the last time interval, T12.

Fig. 5 shows the variation of the normalization of the powerlaw continuum in the 2–10 keV range in the same intervals analyzed in Fig. 2. The normalization changes significantly dur-

**Table 1.** Best fit parameters common to all time intervals

Soft thermal components	
$kT_1$ (mekal)	$0.30^{+0.04}_{-0.03}$ keV
$N_H^{T1}$	$1.88^{+0.8}_{-0.7} 10^{22}$ cm $^{-2}$
$kT_2$ (mekal)	$0.66^{+0.03}_{-0.03}$ keV
$N_H^{T2}$	$0.24^{+0.1}_{-0.1} 10^{22}$ cm $^{-2}$
$kT_3$ (black-body)	$0.16^{+0.02}_{-0.02}$ keV
Powerlaw and reflection components	
$\Gamma$	$1.81^{+0.03}_{-0.06}$
$R_{\text{COLD}}$	$2.6^{+1.0}_{-1.0}$
$R_{\text{ION}}^{\text{in}}$	$0.22^{+0.20}_{-0.10}$
$R_{\text{ION}}^{\text{out}}$	$0.05^{+0.03}_{-0.03}$
Constant absorption components	
$N_{H,1}$	$7.5^{+0.3}_{-0.7} 10^{22}$ cm $^{-2}$
$N_{H,3}$	$3.7^{+1.4}_{-1.0} 10^{24}$ cm $^{-2}$
Emission lines	
$E_N^a$	$6.37^{+0.03}_{-0.03}$ keV
$F_N^a$	$1.25^{+0.1}_{-0.1} 10^{-5}$ keV cm $^{-2}$ s $^{-1}$ keV $^{-1}$
$EW_N^a$	$52^{+4}_{-4}$ eV
$E_B^b$	$6.86^{+0.04}_{-0.04}$ keV
$F_B^b$	$1.2^{+0.1}_{-0.1} 10^{-4}$ keV cm $^{-2}$ s $^{-1}$ keV $^{-1}$
$EW_B^b$	$390^{+40}_{-40}$ eV
$R_{\text{IN}}$	$2.6^{+0.8}_{-0.8} (R_G)$
$R_{\text{OUT}}$	$7.1^{+3.0}_{-2.6} (R_G)$
$\theta^c$	$25^{+15}_{-10}$ deg
$q^d$	$2.9^{+0.9}_{-0.9}$

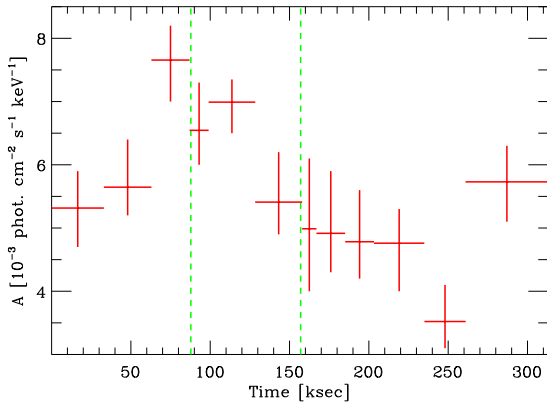
Notes:

<sup>a</sup> Energy, flux and equivalent width of the narrow component of the FeK $\alpha$  line.

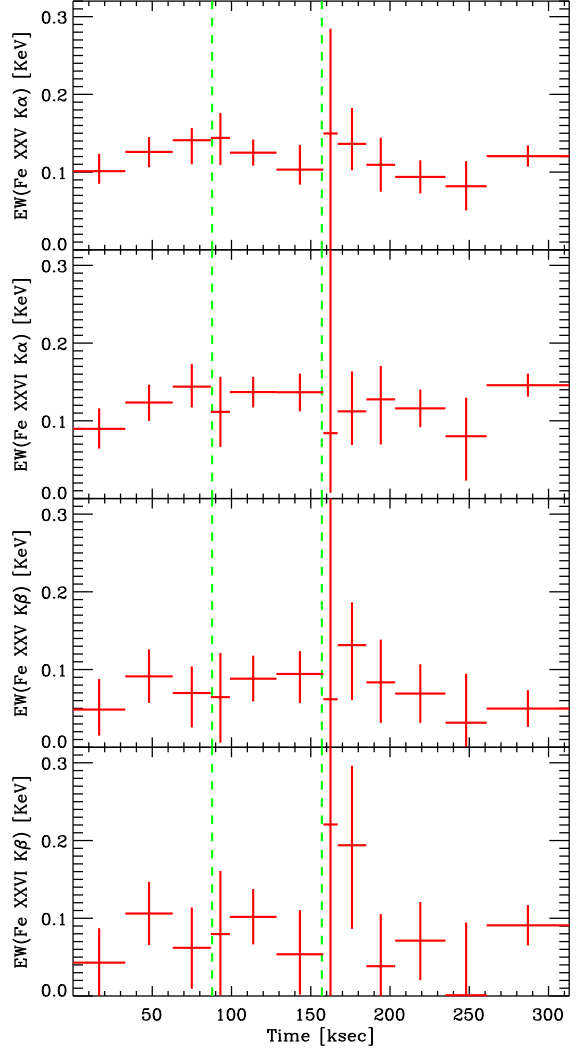
<sup>b</sup> Energy, flux and equivalent width of the broad component of the FeK $\alpha$  line.

<sup>c</sup> Disk inclination angle in the broad line component.

<sup>d</sup> Disk emissivity index in the broad line component.

**Fig. 5.** Variation of the normalization of the powerlaw continuum in the 2–10 keV range over the 12 time intervals analyzed in Sect. 3. The green dashed lines indicate the beginning of eclipses A and B, as in Fig. 2.

ing the observations. This is not unexpected since NGC 1365 is a Narrow Line Sy1 and, as such, it is expected to be characterized by significant variability. It is important to note that the

**Fig. 6.** Equivalent width of the Fe absorption lines over the 12 time intervals analyzed in Sect. 3. The green dashed lines indicate the beginning of eclipses A and B, as in Fig. 2.

variations in the normalization of the powerlaw are uncorrelated with the 2–5 keV light curve behavior, further supporting the idea that the variations of the light curve also require variation of the absorbing column density and covering factor.

Fig. 6 shows the equivalent width of the four Fe absorption lines (FeXXV K $\alpha$  6.697 keV, FeXXVI K $\alpha$  6.966 keV, FeXXV K $\beta$  7.880, FeXXVI K $\beta$  8.268 keV) in the 12 time intervals analyzed in Sect. 3. Although there is some indication of variation of the depth of the absorption lines, especially in association with eclipse B, the variations are all within the statistical errors. Fig. 7 shows the bulk velocity of the absorption lines, which also does not show significant changes within errors. We note that the inferred EW are in line with those obtained for the same source by Risaliti et al. (2005b). In the latter work variability of the lines (both in terms of EW and of velocity) was observed on timescales of a few months. However, our data are not sensitive

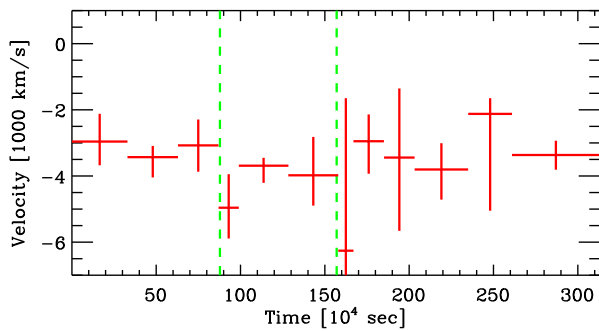


**Fig. 7.** Velocity of the Fe absorption lines over the 12 time intervals analyzed in Sect. 3. The green dashed lines indicate the beginning of eclipses A and B, as in Fig. 2.

to small changes in the absorption lines EW and velocity shift on much shorter timescales, with lower exposures.

#### 4. The cometary shape of the eclipsing clouds

From Fig. 2, and in particular from the light curve and the  $N_{\text{H},2}$  variations, we identify two main eclipsing events, labelled “A” and “B”, due to the passage of two clouds in front of the X-ray source, with eclipse “B” being the more prominent and more clear event. The decreasing  $N_{\text{H},2}$  in the time interval prior to eclipse “A” probably shows the final part of the occultation by a previous cloud. The eclipses are far from being symmetric, implying that clouds are not spherical. A spherical cloud significantly larger than the X-ray source would either produce a sudden total obscuration ( $\text{CF} = 1$ ) or a smooth and symmetrical evolution of the covering factor if grazing the X-ray source; while a spherical cloud with size comparable to, or smaller than the X-ray source would simply produce a short, symmetric dip in the light curve and in the covering factor.

Instead, both eclipses start with an abrupt drop of the 2–5 keV flux (marked by the green vertical dashed lines A and B in Fig. 2) occurring within less than a few thousand seconds. The spectral analysis of the first time interval of each eclipse (Fig. 2b and c) indicates that such a sudden drop of X-ray flux is due to the transit of a cloud with  $N_{\text{H}} \sim 10^{23} \text{ cm}^{-2}$  suddenly covering about 65% of the source. Subsequently the covering factor increases, but more slowly, on time scales of about 50 ksec.

These observational results indicate that the occulting cloud must be elongated, with a size perpendicular to the direction of motion comparable to the X-ray source, while the size along the direction of motion is at least an order of magnitude larger. This is an immediate consequence of the fact that the beginning of the eclipse is very sharp (with the covering factor jumping to 65% in about a ksec) while the subsequent evolution of the covering factor is much smoother on timescales of several 10 ksec.

The fact that the covering factor slowly increases, reaching unity about 50 ksec after the beginning of the eclipse, indicates not only that the clouds are elongated, but that they must have a conical, cometary shape, with their tail gradually occulting the whole X-ray source.

The decrease of column density with time within each eclipse indicates that the head of the “comet” is much denser than its tail, while the latter fades gradually into a low density medium. We note that even the time interval before eclipse “A” shows a similar trend, i.e. decreasing  $N_{\text{H},2}$  and increasing covering factor, hence in these intervals we may be observing the

tail of a comet whose head passed before the beginning of the observation.

We can quantify the geometry of these “cometary” clouds, as discussed in the coming sections. Note however, that their basic scale depends heavily on the clouds’ velocities and on the dimension of the X-ray source, which are both unknown, although some constraints can be set.

The sketch in Fig. 8 summarizes the geometrical constraints inferred for the two clouds derived below. This is obtained under the assumption that the tail is elongated exactly along the direction of motion of the cloud. Moreover, based on the analysis of the temporal variation of the covering factor we can only reconstruct the shape of the cometary tail *projected* on the plane of the sky. Our data cannot probe any elongation of the tail along the line of sight.

In principle the observed variations can be interpreted with other, more complex geometries (e.g. curved clouds with density gradients along the direction of motion), but the cometary shape is the simplest model that can account for both the variations of covering factor and of column density, and which can be interpreted in terms of physically plausible scenarios, as is discussed later on in sect. 8.

##### 4.1. The clouds’ velocity

If we assume that the cloud head is a hemisphere (Fig. 8), then the fact that the initial covering factor of each eclipse is large ( $\sim 65\%$ ), but not total, along with the fact that the initial flux drop is very sharp, indicate that the cometary cloud head and the X-ray source have similar sizes. The sharpness of the flux drop at the beginning of each eclipse provides constraints on the ratio  $R_{\text{X}}/V_{\text{C}}$  between the size of the X-ray source ( $\sim$  size of the cloud head), and the cloud velocity (in the plane of the sky).

Fig. 9 shows the detail of the 2–5 keV light curve around the beginning of eclipse “A”, with a binning of 500 sec (top) and 100 sec (bottom). The gaps are due to the Earth occultation during the *Suzaku* orbit. The sudden flux drop due to the passage of the head of the cloud is marginally resolved, just before the Earth occultation gap, and it lasts about one ksec, or less. We modelled the expected light curve with a simple model where the X-ray source has a radius  $R_{\text{X}}$ , the cometary cloud head is a hemisphere with radius  $R_{\text{head}} \sim R_{\text{X}}$ , moving with a velocity  $V_{\text{C}}$  transverse to the line of sight, and covering 65% of the X-ray source right after the “head” transit. The minimum possible radius for the X-ray source is given by the minimum stable orbit in the case of a maximally rotating black hole, which, in the case of NGC 1365 implies  $R_{\text{X}} > 0.5 R_{\text{S}} = 3 \cdot 10^{11} \text{ cm}$  (sect. 3). This, very conservative, lower limit on the size of the X-ray source, along with the short timescale of the beginning of the eclipse ( $\leq 1 \text{ ksec}$ ), sets a lower limit on the velocity of cloud “A”,  $V_{\text{C}}(\text{A}) > 3000 \text{ km/s}$ . By using these lower limits (i.e.  $R_{\text{X}} = 3 \cdot 10^{11} \text{ cm}$  and  $V_{\text{C}} = 3000 \text{ km/s}$ ) we obtain the light curve shown by the red solid line in Fig. 9. A larger size of the X-ray source would imply a correspondingly higher cloud velocity, with the constraint that  $R_{\text{X}}/V_{\text{C}}(\text{A}) \sim 1 \text{ ksec}$ .

For cloud “B” the eclipse starts within an Earth occultation gap. In this case we can only set an upper limit to the ratio  $R_{\text{X}}/V_{\text{C}}(\text{B}) < 3 \text{ ksec}$ , hence we infer a lower limit on the cloud velocity of  $V_{\text{C}}(\text{B}) > 1000 \text{ km/s}$ , by assuming for  $R_{\text{X}}$  the smallest stable orbit for a maximally rotating black hole.

We note that the lower limit on the velocity of cloud “B” is consistent with the average velocity for BLR clouds inferred from the FWHM of the broad  $\text{H}\beta$  line, i.e. 1900 km/s (Schulz et al., 1999), in agreement with the scenario where the

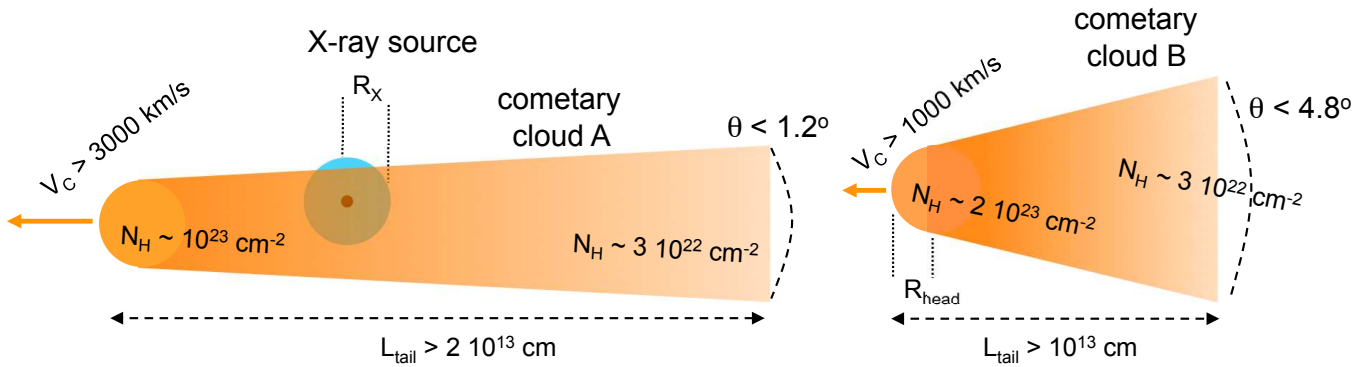


**Fig. 8.** Sketch illustrating the geometry of the cometary clouds that eclipse the X-ray source, as inferred by our observations. For the sake of clarity the drawing dimensions are not in the correct scale (in particular the horizontal length of the tails should be much longer when compared to the size of the cloud heads and the tail opening angles are exaggerated). The variation of the covering factor expected by this model is shown with a dotted line in Fig. 2c.

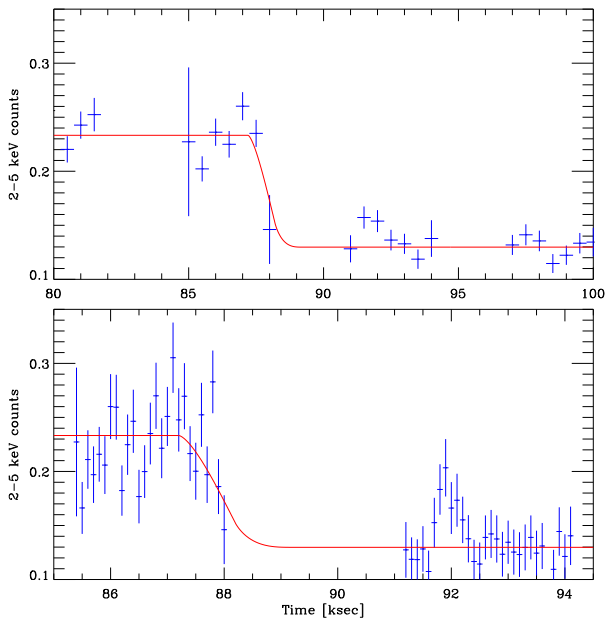


**Fig. 9.** Detail of the 2–5 keV light curve around the beginning of eclipse ‘A’. The top panel is with bins of 500 sec. The bottom panel is with bins of 100 sec and the time axis is further expanded around the beginning of eclipse. The red solid line indicates the modelled light curve where the ratio between the size of the X-ray source ( $\sim$ radius of the cloud head) and the cloud velocity is  $R_X/V_C = 10^8$  cm (km/s) $^{-1}$  (see text). If  $R_X = R_S$  this implies  $V_C = 6000$  km/s.

eclipsing clouds are part of the BLR, as discussed later on in Sect. 6.

For cloud ‘A’ we infer a velocity larger than expected for the average BLR cloud, however not an unrealistic one given that the power law-like profile of the broad lines Nagao et al. (2006) implies a large fraction of clouds with velocity larger than inferred from their FWHM. Yet, if  $R_X \gg R_S$  then the clouds’ velocity is unrealistically large compared with the observed profile of the broad lines.

#### 4.2. The opening angle of the cometary tail

The evolution of the covering factor as a function of time provides constraints on the geometry of the cloud tail. The model used to fit the data (Fig. 8) depends only on two parameters: the initial covering factor ( $\sim 65\%$  both for cloud ‘A’ and ‘B’) and the quantity  $R_X/(V_C \tan \theta_{\text{tail}})$ , where  $\theta_{\text{tail}}$  is the opening angle of the cloud tail. In the case of cloud ‘B’ (where the evolution of the covering factor is better constrained) we obtain  $R_X/(V_C \tan \theta_{\text{tail}}) \sim 35.8$  ksec. The resulting fit to the data is shown with a dotted line in Fig. 2c. This value, along with the upper limit on the ratio  $R_X/V_C(B) < 3$  ksec inferred above, implies an upper limit on the opening angle of the tail of  $\theta_{\text{tail}}(B) < 4.8^\circ$ .

In the case of cloud ‘A’ the evolution of the covering is determined more poorly, due to the larger errors. In this case we can only set an upper limit to the quantity  $R_X/(V_C \tan \theta_{\text{tail}}) > 47.7$  ksec, whose corresponding fit to the data is shown with a dotted line in Fig. 2c. However, as discussed above, in this case we have a better constraint on the ratio  $R_X/V_C(A) \sim 1$  ksec, hence we can obtain a stronger upper limit on the tail opening angle,  $\theta_{\text{tail}}(A) < 1.2^\circ$ .

#### 4.3. The length of the cometary tail

As shown in Fig. 2b, the column density  $N_{H,2}$  of each cloud drops rapidly (the dotted lines represent a simple, empirical quadratic fit to the observed evolution of  $N_{H,2}$ ). The length of the tail is set observationally by our capability to disentangle the cometary cloud absorption from the (constant) global foreground absorber  $N_{H,1}$ , which has a value of  $7.5 \cdot 10^{22}$  cm $^{-2}$  (Table 1). Through simulations we have obtained that our spectra cannot recover a partial absorber with  $N_{H,2} < 2 \cdot 10^{22}$  cm $^{-2}$  (i.e. a factor of  $\sim 10$  below the  $N_{H,2}$  in the head). With this observational ‘definition’, the time elapsed between the passage of the cloud head and the time when  $N_{H,2}$  drops below this limiting value, along with the lower limit on the cloud velocity inferred above, provides a lower limit on the length of the tail:  $L_{\text{tail}}(A) > 2 \cdot 10^{13}$  cm and  $L_{\text{tail}}(B) > 10^{13}$  cm.

### 5. How common are ‘comets’ in AGNs?

In this section we discuss whether the cometary geometry of the clouds observed by us are peculiar to these observations, or to NGC 1365, or whether they may be a more general property of

the absorbing clouds in other AGNs, not so far recognized so far in the data.

NGC 1365 may itself appear a peculiar case, since it is the AGN where the strongest and most frequent  $N_{\text{H}}$  variations have been observed (e.g. Risaliti et al., 2005a, 2007, 2009a). This is partly due to the fact that NGC 1365 is extremely bright in the X-ray band, which is a requirement to properly monitor  $N_{\text{H}}$  variations even on short time scales. Some of the other nearby bright AGNs have indeed displayed  $N_{\text{H}}$  variations on short time scales (Elvis et al., 2004; Puccetti et al., 2007).

However, among the other bright sources, which could in principle allow the same investigation, NGC 1365 probably has a fortunate viewing angle. If the obscuring clouds have a flattened distribution (Elvis, 2000; Risaliti et al., 2002; Maiolino et al., 2001; Gaskell et al., 2007), coplanar with the dusty circumnuclear absorber (Nenkova et al., 2008), then in most type 1 AGNs it is rare to have a cloud transiting along the line of sight. On the other hand, in the classical type 2 AGNs, with equatorial viewing angle, the number of clouds transiting along the line of sight is so large that they make, on average, the absorption nearly constant. NGC 1365, which is a type 1.8 AGNs (Schulz et al., 1999), probably has an intermediate viewing angle, where there are a significant number of clouds transiting the line of sight, but not large enough to average out the  $N_{\text{H}}$  variations. Therefore, in this scenario, NGC 1365 is a particularly good laboratory to investigate clouds through their transits along the line of sight, even though intrinsically it may have no peculiar properties. An alternative possibility is that the density of absorbing clouds surrounding different AGNs vary from object to object (in this scenario the difference between type 2 and type 1 AGN would be mostly due to the number of clouds rather than inclination), and NGC 1365 may have the appropriate density of clouds that makes the probability of detecting eclipses high, but not large enough to average out  $N_{\text{H}}$  variations.

Assessing the detectability of the cometary geometry of the clouds in other objects similar to NGC1365, as well as in other observations of NGC 1365 itself, is not simple. Long ( $> 100$  ksec), continuous observations, like the one reported here, are required to detect the cometary tail in a transiting cloud. This kind of observation is performed rarely. In most cases long integration times are obtained through several, discontinuous short observations (a few 10 ksec each). Even when such data are available the analysis must be tuned to find these types of changes. This involves the complex simultaneous fit over the various time intervals by leaving free both covering factor and  $N_{\text{H}}$  for the variable absorber. Luck also plays a role: 1) the transiting clouds must be moving fast to make the covering factor and  $N_{\text{H}}$  variations easy to identify in terms of a cometary shape; 2) the variation of  $N_{\text{H}}$  and of covering factor must be pronounced, else the two quantities would result in a degenerate fit; 3) if the head of the cloud does not eclipse the X-ray source, and only the tail transits in front of the X-ray source, then the evolution of the light curve and of the covering factor would appear much smoother, and would not be easy to ascribe to the cometary tail.

To our knowledge, the only previous (nearly) continuous, moderately long observations of a bright AGN, with variable obscuration events, are the XMM long observations of NGC 1365 presented in Risaliti et al. (2009a), Risaliti et al. (2009b) and Turner et al. (2008). The observation in Risaliti et al. (2009a) does not show an “eclipsing” event, but rather the uncovering of the X-ray source due to a “hole” in the clouds distribution, hence it is not suitable to trace the geometry of the clouds. In the data of Risaliti et al. (2009b) the variation of  $N_{\text{H},2}$  and CF are much milder than observed in our data; as a consequence, in

Risaliti et al. (2009b) it was not possible to leave both parameters free in all time intervals, since the two quantities would result degenerate. Therefore, in Risaliti et al. (2009b) only the covering factor was left free to vary among the time intervals and details on the structure of the eclipsing cloud could not be inferred. The inferred evolution of the CF during cloud transit appears relatively symmetric, with no obvious evidence for a cometary shape. However, if we had also kept  $N_{\text{H},2}$  constant in our observation, then we would have obtained a more symmetric variation of the covering factor: the decreasing  $N_{\text{H},2}$  obtained by us in the second part of each eclipse (Fig. 2) would be interpreted (with a worse  $\chi^2$ ) as a decreasing covering factor in a model where  $N_{\text{H},2}$  is kept constant. Therefore, the eclipse observed in the XMM observation may also be cometary-like, but the adopted model may have prevented its identification. Yet, the light curve of the long XMM observation does not show the sharp flux drop observed at the beginning of our eclipses “A” and “B”. This may be either due to the fact that the cloud in the XMM observation was moving more slowly (hence the eclipse transition was much smoother in time), or to the fact that the head of the cometary cloud did not pass in front of the X-ray source (hence only the smoother occultation produced by its tail was observed), or more simply because the cloud head was “fuzzier”.

Similar considerations apply to the eclipse identified by Turner et al. (2008), which was not modelled in terms of both variable covering factor *and* variable  $N_{\text{H}}$ , and whose light curve does not show a sharp flux drop, as in Risaliti et al. (2009b).

However, sharp drops of the X-ray flux in few ksec (similar to those observed at the beginning of eclipses “A” and “B”), have been observed in previous observations of other AGNs. McKernan & Yaqoob (1998) investigated in detail one such drop in an ASCA observation of MCG-6-30-15, which they ascribed to the occultation of the X-ray source by a “symmetric” cloud. However, they could not investigate the spectral evolution of this occultation, which is required to infer the presence of a cometary tail. By only using the light curve the beginning of our eclipse “A” would be interpreted as an occultation by a nearly symmetric cloud; only the investigation of the spectral evolution reveals the cometary shape.

Finally, we mention that our team has found evidence for cometary clouds also in another source (Risaliti et al. 2010, submitt.) through the detailed temporal analysis of X-ray data.

Summarizing, the cometary shape could be a common property of the X-ray obscuring clouds in general. However, this feature is difficult to identify if the observations are not adequate or the source not bright enough, so the occurrence rate is presently unknown.

## 6. Cometary clouds as BLR clouds

Several papers have discussed that rapid changes (days-hours) of the absorbing column density in AGNs support a location of the associated absorbing clouds within the radius of the Broad Line Regions (Elvis et al., 2004; Puccetti et al., 2007; Risaliti et al., 2005a, 2007, 2009a,b). The rapidly variable absorption in our *Suzaku* data can also be ascribed to BLR clouds. In the following we provide a more quantitative justification of this scenario.

We assume that the absorbing clouds are in Keplerian rotation around the supermassive black hole. In the case of a spherical cloud crossing the line of sight (with the X-ray source smaller or comparable to the projected size of the cloud), the distance  $D$  of the absorber from the black hole can be inferred from the

crossing time, traced by the absorption variation, through the equation (Risaliti et al., 2002)

$$D \sim 6 \cdot 10^{26} t_{\text{cr}}^2 n_{\text{cl}}^2 N_{\text{H}}^{-2} R_{\text{S}} \text{ [cm]} \quad (1)$$

where  $t_{\text{cr}}$  is the crossing time in units of ksec,  $n_{\text{cl}}$  is the cloud density, in units of  $\text{cm}^{-3}$ , and  $N_{\text{H}}$  its column density, in units of  $\text{cm}^{-2}$ . In our case clouds are certainly not spherical. However, we can approximate the dense “head” of the cometary clouds with hemispheres, as discussed above. In this case  $t_{\text{cr}}$  is twice the transition interval at the beginning of the eclipses, i.e.  $t_{\text{cr}} \sim 4$  ksec (by taking the average of clouds A and B, Sect. 4.1). For the column density of the heads we can assume the average of those observed at the beginning of eclipses A and B, i.e.  $N_{\text{H}} \sim 1.5 \cdot 10^{23} \text{ cm}^{-2}$ . The gas density of the cloud can be roughly estimated by assuming  $R_{\text{head}} \geq R_{\text{S}} \sim 6 \cdot 10^{11} \text{ cm}$  (as justified in Sect. 4), hence  $n_{\text{cl}} = n_{\text{head}} \lesssim N_{\text{H}}/2R_{\text{head}} \sim 10^{11} \text{ cm}^{-3}$ . In this case Eq. 1 gives  $D \lesssim 2 \cdot 10^{15} \text{ cm}$ . This value is consistent with that inferred by (Risaliti et al., 2009b) through an independent analysis of other eclipsing events.

Although this is an approximate estimate, given the various assumptions involved, it is within the radius of the BLR inferred for NGC 1365. Indeed, by using the  $R_{\text{BLR}} - L_{\text{X}}$  relation given in Kaspi et al. (2005) and the intrinsic X-ray luminosity inferred in (Risaliti et al., 2009c, adapted to our new slope),  $L_{2-10\text{keV}} \sim 5 \cdot 10^{42} \text{ erg s}^{-1}$ , we infer a radius of the broad line region of  $R_{\text{BLR}} \sim 10^{16} \text{ cm}$ . This result strongly supports the scenario identifying the cometary clouds found in the *Suzaku* data with BLR clouds. It should be noted that the BLR radius given by the relation in Kaspi et al. (2005) refers to the clouds predominantly emitting  $\text{H}\beta$ . However, the radius of the BLR actually spans about an order of magnitude as inferred by reverberation studies (Kaspi & Netzer, 1999), with high ionization lines being emitted predominantly in the inner BLR while low ionization lines predominantly coming from the outer region. The distance inferred for the absorbers ( $D \lesssim 2 \cdot 10^{15} \text{ cm}$ ), relative to the BLR radius inferred for the  $\text{H}\beta$  emitting clouds, suggests that the absorbers observed by us are mostly associated with the high-ionization clouds (e.g. those emitting CIV).

We can infer the mass of individual clouds based on the density inferred above. In particular the “head” of the clouds has a mass of  $M_{\text{head}} \geq n_{\text{head}} m_{\text{H}} \frac{4}{3} \pi R_{\text{head}}^3 \sim 4 \cdot 10^{-11} M_{\odot}$  (here we have assumed that the cloud head is a full sphere, whose leading hemisphere is probed by the observed variations of  $N_{\text{H}}$  and CF, while the trailing hemisphere is observationally confused within the cometary tail). For what concerns the tail, given its small opening angle we can approximate  $R_{\text{tail}} \sim R_{\text{head}} \sim R_{\text{X}} \geq R_{\text{S}} = 6 \cdot 10^{11} \text{ cm}$ . We can infer the density of the tail by assuming that the cross section of the tail is axi-symmetric relative to the direction of motion, hence  $n_{\text{tail}} \sim N_{\text{H,tail}}/R_{\text{tail}} \lesssim 10^{10} \text{ cm}^{-3}$  (Fig. 2). Out to the length that we can detect through our observations (Figs. 2-8) we infer a mass of the tail of  $M_{\text{tail}} \geq n_{\text{tail}} m_{\text{H}} \pi R_{\text{tail}}^2 L_{\text{tail}} \sim 10^{-10} M_{\odot}$ .

From the mass of individual clouds we can derive the mass of the BLR if the density of clouds is known. The latter can be inferred from the frequency of the eclipsing events. Our and past observations of NGC 1365 display eclipses in  $\sim 1/3$  of the monitoring time, implying that about one hundred of absorbing clouds must be present in the volume,  $\mathcal{V}$ , probed by our line of sight toward the X-ray emitting source in one year, within the region hosting the absorbers. We can write  $\mathcal{V} \sim 2R_{\text{head}} (V_{\text{C}} \cdot 1\text{yr}) D \sim 5 \cdot 10^{-13} \text{ pc}^3$ , where we have assumed  $V_{\text{C}} = 2000 \text{ km s}^{-1}$  and  $D \sim 2 \cdot 10^{15} \text{ cm}$  as representative of the clouds velocity and of their distance to the center (as discussed above). The inferred volume density of the absorbers is

therefore  $100/\mathcal{V} \sim 2 \cdot 10^{14} \text{ pc}^{-3}$ . If we assume that this density is uniform within the radius of the BLR, then we obtain a total number of clouds of about  $N_{\text{C}} \sim 3 \cdot 10^7$ .

The total mass of the BLR inferred from the properties of the absorbers is  $M_{\text{BLR}}^{\text{abs}} \approx N_{\text{C}} (M_{\text{head}} + M_{\text{tail}}) \approx 4 \cdot 10^{-3} M_{\odot}$ . The latter value is five orders of magnitude lower than inferred from photoionization models. Indeed, according to Baldwin et al. (2003), the mass of the BLR inferred from photoionization models scales as  $M_{\text{BLR}}^{\text{phot}} \approx 2 \cdot 10^{-44} (\nu L_{\nu})_{1450\text{\AA}} M_{\odot}$  (note that we do not use the monochromatic luminosity as in Baldwin et al., 2003). Assuming  $(\nu L_{\nu})_{1450\text{\AA}}/L_{2-10\text{keV}} \sim 7$  (Young et al., 2010; Richards et al., 2006), for NGC 1365 we obtain  $M_{\text{BLR}}^{\text{phot}} \approx 0.7 M_{\odot}$ . Accounting for such discrepancy is not easy. One possibility is that the X-ray source is much larger than assumed by us ( $R_{\text{head}} \approx R_{\text{X}} \gg R_{\text{S}}$ ). The inferred density of absorbers scales as  $\sim 1/R_{\text{X}}$ , while the mass of individual clouds scales as  $\sim R_{\text{X}}^2$ , therefore the mass of the BLR inferred from the absorbers scales as  $\sim R_{\text{X}}$ . However, to obtain  $M_{\text{BLR}}^{\text{abs}}$  similar to  $M_{\text{BLR}}^{\text{phot}}$  would require  $\sim R_{\text{X}} = 200 R_{\text{S}}$ , not easy to account for by standard models. Moreover, as discussed in sect. 4.1,  $R_{\text{X}} \gg R_{\text{S}}$  would imply clouds’ velocities unrealistically high relative to those inferred from the broad lines profile.

Alternatively, a significant fraction of the BLR may not be accounted for by the rapidly variable absorbers detected here. We may be biased towards the detection of “small clouds”, simply because the “eclipses” method favors the detection of clouds with size similar to the X-ray source; larger clouds may well exist, but may be more difficult to detect through  $N_{\text{H}}$  variations. In particular, part of the “constant” absorber ( $N_{\text{H},1} = 7.5 \cdot 10^{22} \text{ cm}^{-2}$ ) may be associated with much larger clouds in the BLR (possibly located in the outer part), whose  $N_{\text{H}}$  variability is only detected on much longer timescales (e.g. see Risaliti et al., 2009a,b). The mass of such large clouds may account for the bulk of the mass of the BLR.

Yet another possibility is that the mass of the BLR clouds inferred by photoionization models may be erroneously (over-)estimated. Indeed, such models assume that the photoionization is due to a nuclear point-like source (the accretion disk). However, as discussed in the next section, part of the photoionizing flux may be produced *locally* by the shock generated by the interaction between the clouds and the diffuse intracloud medium. This is expected to significantly relax the requirements of classical BLR photoionization models in terms of mass.

## 7. Dynamics and fate of the cometary clouds

The differential velocity of the gas in the tail relative to the head ( $V_{\text{head}} - V_{\text{tail}}$ ) is simply given by the sound speed of the gas in the cloud ( $\sim 10 \text{ km/s}$ ), since behind the head there is no hot intracloud medium (“cleaned” by the passage of the head), nor other agents preventing the gas from expanding freely. Essentially, the tail follows the head in its motion, and lags behind only by a small fraction of the bulk velocity.

We can estimate the cloud mass-loss through the tail, which is given by

$$\dot{M}_{\text{head}} = (V_{\text{head}} - V_{\text{tail}}) n_{\text{tail}} m_{\text{H}} \pi R_{\text{tail}}^2 \quad (2)$$

We obtain a mass-loss rate of about  $\dot{M}_{\text{head}} \approx 3 \cdot 10^{-10} M_{\odot} \text{ yr}^{-1}$ . By comparison with the mass of the clouds head inferred in the previous section we infer a lifetime of the clouds of  $t_{\text{life}} \approx 2$  months, i.e. shorter than their orbital period (1yr). A similar conclusion on the short lifetime of BLR clouds was reached also by Mathews & Ferland (1987) based on the expected interaction of

BLR clouds with the warm intracloud medium (this issue will be discussed further in the next section).

The latter constraint has important implications. The BLR in most type 1 AGNs is observed to be present (and often nearly constant) for more than 10-20 years. As a consequence, the much shorter lifetime of the BLR clouds implies that they have to be continuously replenished, and at a very small radius ( $< 10^{16}$  cm). Direct infall at such small radii is unlikely (inflow must occur through the accretion disk). The more likely possibility is that BLR clouds are continuously produced by the accretion disk, as suggested by the model in Elvis (2000).

It should be noted that  $t_{\text{life}}$  depends on our assumption on  $R_X$ , since  $\dot{M}_{\text{head}}/\dot{M}_{\text{head}}$  depends linearly on  $R_{\text{head}} \sim R_X$ . However, to make the lifetime of the absorbing clouds longer than several years (to account for the observationally continuous presence and “stability” of the BLR) would require  $R_X \gg R_S$ , which runs into other physical problems discussed in sect. 6. Yet, within this context, we note that the argument on the short timescale only applies to the “small” cometary clouds detected through the short timescale  $N_H$  variability. The putative larger BLR clouds mentioned in the previous section may not suffer the same timescale problem if they are much more massive.

The global mass loss of BLR comets is  $\dot{M}_{\text{tot}} = N_C \dot{M}_C \sim 10^{-2} M_{\odot} \text{ yr}^{-1}$ . Modelling the fate of such gas lost by the comets is very difficult and goes beyond the scope of this paper. Here we only mention two possibilities. If the density drops significantly, the effective ionization parameter may become high enough to make the gas thermally unstable and heating up to  $10^7$  K, hence contributing to the hot intracloud medium (see next section). The gas lost by the cometary clouds may also be accelerated by the radiation pressure contributing to a fraction of the wind often observed in Seyfert nuclei, and whose outflow rate is generally estimated to be around  $0.1 M_{\odot} \text{ yr}^{-1}$  (Krongold et al., 2007; Crenshaw et al., 2003; Andrade-Velázquez et al., 2010).

## 8. The nature of the cometary clouds

It is beyond the scope of the present work to define a detailed physical model accounting for the nature of the “cometary-like” structure of the clouds. In this section we only try to identify the most plausible scenarios, by exploiting the constraints provided by the observations discussed in the previous sections. As discussed above, these cometary clouds are most likely part of the BLR. Therefore, any discussion on their nature is necessarily interlaced with the nature of the BLR clouds in general, which is still matter of debate (see Netzer, 2008, for a review), although here we mostly focus on their cometary shape.

First, although we use the term “comets”, these are not comets in the solar system sense, i.e. their tail is not due to radiation pressure on the gas. Indeed, the latter would make the tail elongated radially and yielding symmetric variations of the  $N_H$  and of the covering factor, in contrast to what is observed. Yet, as mentioned in sect. 4 we cannot exclude a component of the tail elongated along our line of sight.

In Sect. 6 we inferred that each cloud head must have a gas density of about  $10^{11} \text{ cm}^{-3}$ , while the density drops by about an order of magnitude along the tail. The large density of the head may suggest that we are actually seeing the (bloated) atmosphere of a star passing along the line of sight. Models ascribing the BLR clouds to the atmosphere of (bloated or evolved) stars have been proposed in the past (Scoville & Norman, 1988; Alexander & Netzer, 1994, 1997) and it was also suggested that such stellar atmospheres may produce contrails (Scoville & Norman, 1995), which may mimic

the “tails” observed in our clouds. However, as discussed in sect. 6, the inferred density of the absorbing clouds ( $\sim 10^{14} \text{ pc}^{-3}$ ) is by far larger than the stellar density in the center of galaxies. In the light of the present X-ray observations, modelling the BLR structure in terms of stellar atmospheres seems not to be a physically viable interpretation. The absorbing (and BLR) clouds are likely purely gaseous (non self-gravitating) objects. Yet, we cannot exclude that *some* of the eclipsing events are due to transiting stellar atmospheres.

Within the general framework of AGN central regions, these “cometary-clouds” should be moving through a diffuse, (relatively) hot intracloud medium (HIM), as originally discussed in Krolik et al. (1981). This scenario has been subject to revisions and objections and, at present, the temperature of such diffuse medium is estimated to be  $T_{\text{HIM}} \sim 10^7$  K (Perry & Dyson, 1985; Fabian et al., 1986; Collin-Souffrin et al., 1988; Netzer, 1990; Krolik, 1999). This intracloud medium might well be in outflow, but it is highly unlikely that such medium is in orbital motion around the central black hole, so that we can exclude that the absorbing clouds with the inferred velocities are co-moving with this ambient medium (at least for what concerns the orbital component of their motion). A simple estimate of the HIM sound speed shows that these cometary clouds must indeed be moving supersonically through the HIM. In fact, the sound speed in the HIM is  $(c_s)_{\text{HIM}} \sim 290 (T_{\text{HIM}}/10^7)^{1/2} \text{ km s}^{-1}$ , while the inferred velocities of the “cometary” clouds are significantly larger (Sect. 4.1). The inferred Mach numbers are  $M_A > 20$  and  $M_B > 7$  (recall that only lower limits on the clouds velocities were obtained in Sect. 4.1). These imply Mach cones with opening angles ( $< 1.5^\circ$  and  $< 4^\circ$  for clouds A and B, respectively) consistent with the tails opening angles inferred by us through the variation of the covering factor.

The supersonic motion of dense clouds in a less dense medium has been extensively studied in the past, although mostly in very different astrophysical contexts (Falle et al., 2002; Pittard et al., 2005a,b). Such theoretical studies show that in general a sort of (“cometary”) tail, behind the front shock does indeed tend to form. In numerical simulations the specific result (shape, physical properties, etc...) depends on the particular physical processes accounted for (for example, whether radiative cooling is included or not) and on the physical parameters, especially on the density contrast between unshocked ambient medium and cloud material, and on the Mach number. In any case, a system of front shocks (bow-shock like) at the head of the cloud, and a sort of Mach cone, prolonging the bow-shock at the rear of the cloud-head itself, must form. The “cometary tail” is made up by the debris of trailing material lost by the cloud head, because of the action both of Rayleigh-Taylor and Kelvin-Helmholtz instabilities (Krolik et al., 1981; Mathews & Ferland, 1987) and of other possible disrupting mass loss mechanisms (e.g. Pittard et al., 2005b, and reference therein). Moreover, as discussed above, the lack of a confining medium on the trailing side of the cloud head naturally leads to gas loss at the sound speed ( $\sim 10 \text{ km/s}$ ) due to free expansion, even in absence of any hydrodynamical instability. An elongated structure, trailing behind the cloud denser head, is therefore expected by models, and also with a cometary-shape. However, a more quantitative comparison with our data is extremely complex, since it requires that such models are modified to match the physical conditions observed in AGNs and in NGC 1365 in particular.

It is important to note that, as first pointed out by Collin-Souffrin et al. (1988), the shock generated by the supersonic motion of the BLR clouds into the HIM is expected to generate UV and X-ray radiation that can contribute significantly to

the ionization *in situ* of the cloud itself. This effect requires a substantial revision of the classical photoionization models of the BLR, which assume photoionization by a nuclear, point-like radiation source.

Finally, we mention that magnetic fields can provide an additional mechanism that could elongate the circumnuclear clouds into a filamentary, and possibly cometary, shape. Strong magnetic fields are expected to surround accreting black holes, and have been proposed as an alternative mechanism to confine the BLR clouds (Rees, 1987; Ferland & Rees, 1988), with the effect of making them elongated along the field. Inferring the actual shape of the clouds expected to originate from such a mechanism is also very complex and beyond the scope of this paper, a more detailed analysis of these effects is deferred to a future paper. Here we only note that the past models of magnetically confined BLR clouds do predict elongated structures, but do not obviously predict dense heads as those observed here.

## 9. Summary

We have presented a detailed spectral analysis of a long ( $\sim 300$  ksec), continuous *Suzaku* observation of the Seyfert nucleus in the galaxy NGC 1365. The spectrum shows evidence for an absorption component that is variable in time, both in terms of column density and in terms of covering factor, which is ascribed to clouds eclipsing the X-ray source. This is the first time that a temporally resolved X-ray spectral analysis is able to break the degeneracy between the evolution of the column density ( $N_H$ ) and the covering factor (CF) of the X-ray absorber.

We identify two main eclipses. The temporal evolution of each eclipse is far from being symmetrical. The initial occultation is very rapid (within  $\sim 1$  ksec) and covering about 65% of the source. Subsequently the covering factor increases, but more slowly, reaching unity in about 50 ksec. The absorbing column density of the cloud is about  $10^{23}$   $\text{cm}^{-2}$  at the beginning of each eclipse and decreases afterwards. These results are inconsistent with a spherical geometry for the absorbing clouds. The most likely geometry compatible with the observations is an elongated, “cometary” shape, with a dense “head” ( $n \sim 10^{11}$   $\text{cm}^{-3}$ , consistent with that expected for the clouds of the BLR) and with a dissolving and expanding tail.

The data allow us to quantitatively constrain the geometry, dynamics and location of such cometary clouds. The cometary clouds are probably located at a distance of about  $2 \cdot 10^{15}$  cm from the nuclear black hole, well within the estimated BLR radius ( $\sim 10^{16}$  cm), strongly supporting the association of these absorbing systems with BLR clouds (at least with the inner, high-ionization ones). The cometary clouds “head” must have a size comparable to the X-ray source and must be moving with velocity higher than about 1000 km/s (consistent with the velocity expected for the BLR clouds). The cometary tail must be longer than a few times  $10^{13}$  cm. The tail opening angle must be very narrow, less than a few degrees, and consistent with the opening angle of the Mach cone expected from the supersonic motion of the cloud into the hot intracloud medium.

We suggest that such cometary clouds may be common to most AGNs, but have been difficult to recognize in previous X-ray observations.

We estimate that the cloud “head” loses a significant fraction of its mass through the cometary tail, which is expected to cause the total cloud destruction within a few months. If these clouds are representative of most BLR clouds (or at least the high-ionization ones), our result implies that the BLR region

must be continuously replenished with gas clouds, possibly from the accretion disk.

We briefly discussed the possible nature of such cometary clouds. The most likely scenario is that the tail is made of gas lost by the cloud head through hydrodynamical instabilities generated by its supersonic motion through the hot intracloud medium.

We can estimate the mass of the absorbing clouds ( $M_{\text{cloud}} \sim 10^{-10} M_{\odot}$ ) and their total number within the central region ( $N_C \sim 3 \cdot 10^7$ ). The inferred total mass of the BLR is about  $4 \cdot 10^{-3} M_{\odot}$ , which is two orders of magnitude lower than the BLR mass inferred from photoionization models. The discrepancy may originate from a population of large, massive BLR clouds not identified in our eclipsing studies. Alternatively, photoionization models may overestimate the BLR mass. In particular, UV and X-ray radiation produced by the shocks generated by the supersonic motion of the clouds may provide a local source of ionizing photons, not accounted for by classical photoionization models that assume a central point-like radiation source.

*Acknowledgements.* We are grateful to A. Marconi and to C. Perola for useful discussions. This work was partially supported by INAF and by ASI.

## References

- Alexander, T., & Netzer, H. 1994, MNRAS, 270, 781  
 Alexander, T., & Netzer, H. 1997, MNRAS, 284, 967  
 Andrade-Velázquez, M., Krongold, Y., Elvis, M., Nicastro, F., Brickhouse, N., Binette, L., Mathur, S., & Jiménez-Bailón, E. 2010, ApJ, 711, 888  
 Baldwin, J. A., Ferland, G. J., Korista, K. T., Hamann, F., & Dietrich, M. 2003, ApJ, 582, 590  
 Collin-Souffrin, S., Dyson, J. E., McDowell, J. C., & Perry, J. J. 1988, MNRAS, 232, 539  
 Crenshaw, D. M., Kraemer, S. B., & George, I. M. 2003, ARA&A, 41, 117  
 Elvis, M. 2000, ApJ, 545, 63  
 Elvis, M., Risaliti, G., Nicastro, F., Miller, J. M., Fiore, F., & Puccetti, S. 2004, ApJ, 615, L25  
 Fabian, A. C., Guilbert, P. W., Arnaud, K. A., Shafer, R. A., Tennant, A. F., & Ward, M. J. 1986, MNRAS, 218, 457  
 Falle, S. A. E. G., Coker, R. F., Pittard, J. M., Dyson, J. E., & Hartquist, T. W. 2002, MNRAS, 329, 670  
 Ferland, G. J., & Rees, M. J. 1988, ApJ, 332, 141  
 Gaskell, C. M., Klimek, E. S., & Nazarova, L. S. 2007, arXiv:0711.1025  
 Guainazzi, M., Risaliti, G., Nucita, A., Wang, J., Bianchi, S., Soria, R., & Zezas, A. 2009, A&A, 505, 589  
 Kaspi, S., & Netzer, H. 1999, ApJ, 524, 71  
 Kaspi, S., Maoz, D., Netzer, H., Peterson, B. M., Vestergaard, M., & Jannuzi, B. T. 2005, ApJ, 629, 61  
 Koyama, K., et al. 2007, PASJ, 59, 23  
 Krolik, J. H., McKee, C. F., & Tarter, C. B. 1981, ApJ, 249, 422  
 Krolik, J. H. 1999, Active galactic nuclei : from the central black hole to the galactic environment / Julian H. Krolik. Princeton, N. J. : Princeton University Press, c1999.,  
 Krongold, Y., Nicastro, F., Elvis, M., Brickhouse, N., Binette, L., Mathur, S., & Jiménez-Bailón, E. 2007, ApJ, 659, 1022  
 Maiolino, R., Salvati, M., Marconi, A., & Antonucci, R. R. J. 2001, A&A, 375, 25  
 Mathews, W. G., & Ferland, G. J. 1987, ApJ, 323, 456  
 McKernan, B., & Yaqoob, T. 1998, ApJ, 501, L29  
 Mitsuda, K., et al. 2007, PASJ, 59, 1  
 Nenkova, M., Sirocky, M. M., Nikutta, R., Ivezić, Ž., & Elitzur, M. 2008, ApJ, 685, 160  
 Netzer, H. 1990, Active Galactic Nuclei, 57  
 Netzer, H. 2008, New Astronomy Review, 52, 257  
 Nagao, T., Marconi, A., & Maiolino, R. 2006, A&A, 447, 157  
 Perry, J. J., & Dyson, J. E. 1985, MNRAS, 213, 665  
 Pittard, J. M., Dyson, J. E., Falle, S. A. E. G., & Hartquist, T. W. 2005, MNRAS, 361, 1077  
 Pittard, J. M., Dobson, M. S., Durisen, R. H., Dyson, J. E., Hartquist, T. W., & O’Brien, J. T. 2005, A&A, 438, 11  
 Puccetti, S., Fiore, F., Risaliti, G., Capalbi, M., Elvis, M., & Nicastro, F. 2007, MNRAS, 377, 607  
 Rees, M. J. 1987, MNRAS, 228, 47P

- Richards, G. T., et al. 2006, *ApJS*, 166, 470
- Risaliti, G., Maiolino, R., & Bassani, L. 2000, *A&A*, 356, 33
- Risaliti, G., Elvis, M., & Nicastro, F. 2002, *ApJ*, 571, 234
- Risaliti, G., Elvis, M., Fabbiano, G., Baldi, A., & Zezas, A. 2005, *ApJ*, 623, L93
- Risaliti, G., Bianchi, S., Matt, G., Baldi, A., Elvis, M., Fabbiano, G., & Zezas, A. 2005, *ApJ*, 630, L129
- Risaliti, G., Elvis, M., Fabbiano, G., Baldi, A., Zezas, A., & Salvati, M. 2007, *ApJ*, 659, L111
- Risaliti, G., et al. 2009, *MNRAS*, 393, L1
- Risaliti, G., et al. 2009, *ApJ*, 696, 160
- Risaliti, G., et al. 2009, *ApJ*, 705, L1
- Scoville, N., & Norman, C. 1988, *ApJ*, 332, 163
- Scoville, N., & Norman, C. 1995, *ApJ*, 451, 510
- Schulz, H., Komossa, S., Schmitz, C., & Mücke, A. 1999, *A&A*, 346, 764
- Soria, R., Risaliti, G., Elvis, M., Fabbiano, G., Bianchi, S., & Kuncic, Z. 2009, *ApJ*, 695, 1614
- Turner, T. J., Reeves, J. N., Kraemer, S. B., & Miller, L. 2008, *A&A*, 483, 161
- Turner, T. J., Miller, L., Kraemer, S. B., Reeves, J. N., & Pounds, K. A. 2009, *ApJ*, 698, 99
- Wang, J., Fabbiano, G., Elvis, M., Risaliti, G., Mazzarella, J. M., Howell, J. H., & Lord, S. 2009, *ApJ*, 694, 718
- Young, M., Elvis, M., & Risaliti, G. 2010, *ApJ*, 708, 1388